System design and implementation of the detector assembly of the Astro-H soft x-ray spectrometer

Meng P. Chiao
Joseph Adams
Phillip Goodwin
Clair W. Hobson
Caroline Anne Kilbourne
Daniel McCammon
Daniel S. McGuinness
Samuel J. Moseley
Frederick S. Porter
Sandy Shuman
Tomomi Watanabe

SPIE.

System design and implementation of the detector assembly of the Astro-H soft x-ray spectrometer

Meng P. Chiao,[a,*] Joseph Adams,[a] Phillip Goodwin,[a] Clair W. Hobson,[a] Caroline Anne Kilbourne,[a] Daniel McCammon,[b] Daniel S. McGuinness,[a] Samuel J. Moseley,[a] Frederick S. Porter,[a] Sandy Shuman,[a] and Tomomi Watanabe[a]

[a]NASA Goddard Space Flight Center, Greenbelt, Maryland, United States
[b]University of Wisconsin, Department of Physics, Madison, Wisconsin, United States

Abstract. The soft x-ray spectrometer (SXS) on-board Astro-H presents to the science community unprecedented capability (<7 eV full width half max at 6 keV) for high-resolution spectral measurements in the range of 0.5 to 12 keV to study extended celestial sources. At the heart of the SXS is the x-ray calorimeter spectrometer (XCS) where detectors (calorimeter array and anticoincidence detector) operate at 50 mK, the bias circuit operates at nominal 1.3 K, and the first stage amplifiers operate at 130 K, all within a nominal 20-cm envelope. The design of the detector assembly (DA) in the XCS originates from the Astro-E x-ray spectrometer (XRS) and lessons learned from Astro-E and Suzaku. After the production of our engineering model, additional changes were made to improve our flight assembly process for better reliability and overall performance. We present the final design and implementation of the flight DA, compare its parameters and performance with Suzaku's XRS, and list susceptibilities to other subsystems as well as our lessons learned. © *The Authors. Published by SPIE under a Creative Commons Attribution 4.0 Unported License. Distribution or reproduction of this work in whole or in part requires full attribution of the original publication, including its DOI.* [DOI: 10.1117/1.JATIS.4.2.021404]

Keywords: detector assembly; soft x-ray spectrometer; calorimeter; Astro-H.

Paper 17045SSP received Jul. 29, 2017; accepted for publication Feb. 19, 2018; published online Mar. 19, 2018.

1 Introduction

Hitomi, also known as Astro-H, was launched successfully on February 17, 2016, from the Japan Aerospace Exploration Agency (JAXA) Tanegashima Space Center and had excellent performance during the instrument commissioning phase.

NASA provided the calorimeter spectrometer insert (CSI) and worked closely with Sumitomo Heavy Industry (SHI) Quantum Group Niihama division and JAXA on integration into the flight dewar in the SHI cleanroom facility. The final assembly of the CSI in the SHI dewar is shown in Fig. 1. Various aspects of the soft x-ray spectrometer (SXS) such as in-orbit performance and other subsystems including the dewar will be described in detail elsewhere in this proceeding.[1–17] The CSI includes the detector subsystem (DS) and the adiabatic demagnetization refrigerator (ADR) subsystem. The DS includes the microcalorimeter detector array, the anticoincidence detector, and the detector assembly (DA). Details of the ADR subsystem are discussed by Shirron et al.[3] Details of the DS requirements were published in 2010.[18]

The microcalorimeter detector array for Astro-H is a 6×6 array initially developed for Suzaku XRS with a pixel size of 814 μm on an 832-μm pitch. Each microcalorimeter detector is a thermal detector, which measures minute temperature rises in its thermally linked x-ray absorber at the arrival of x-ray photons, and operates at cryogenic temperature, in this case 50 mK. The x-ray absorbers are 8.5-μm-thick HgTe provided by EPIR. Each is attached by hand to the microcalorimeter detector. The anticoincidence detector is a low-voltage silicon ionization detector of size 1 cm $\times$ 1 cm $\times$ 0.5 mm underneath the microcalorimeter array for screening background charged particle events. The anticoincidence detector operates at the same temperature as the microcalorimeters. Details on the microcalorimeter array and anticoincidence detector are discussed by Kilbourne et al.[1] The DA, shown in Fig. 2, provides the electrical, mechanical, and thermal infrastructure for the calorimeter array and the anti-coincidence detector at the core of the dewar.

Similar to Suzaku, the DA utilizes a modular design and includes four temperature regions as shown in the block diagram in Fig. 3 such as the calorimeter thermal sink (CTS) at 50 mK, the midsection, cover shield, amplifier boxes, and bias box at about 1.3 K, the junction field transistor (JFET) amplifiers at 130 K, and a heat intercept, including the inner JFET boxes, transition cables, thermal straps, and circuit boards at 26 to 28 K. Multistage suspension by Kevlar® threads is used to achieve mechanical support and thermal isolation between modules. The fundamental resonance frequency within each module is designed to be higher than the detector signal band. Electrical wiring within each module is designed to minimize thermal conduction between interfaces, and every wire is under tension to keep microphonic noise outside the detector signal band. Figure 4 shows simplified circuit schematics for the calorimeter and the anticoincidence detector. The x-ray amplifier box (XBOX) and the DS together complete the analog circuits. Both the calorimeter and the anticoincidence detectors use JFETs as the first stage amplifier. The XBOX provides power to the detectors and JFETs and amplifies and digitizes the detector signals or waveforms. The pulse shape processor (PSP) provides commands to the XBOX and processes the digitized waveforms from the XBOX via the optimal filter method for pulse height, arrival time, event grade, and rise time. Overall detector

*Address all correspondence to: Meng P. Chiao, E-mail: meng.p.chiao@nasa .gov
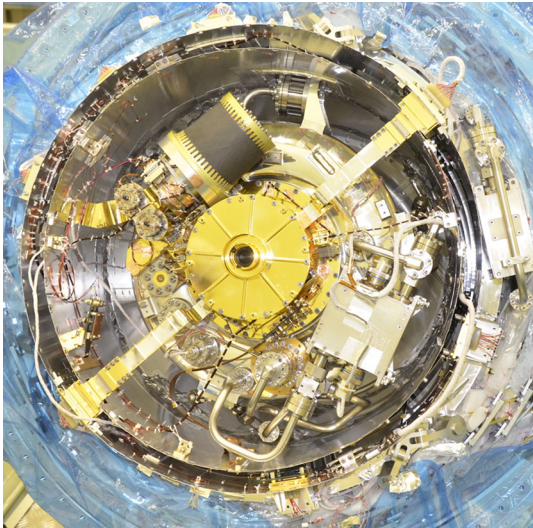
Fig. 1 The CS insert fully integrated in the Astro-H flight dewar is shown at the center of the figure with a nonflight, alignment fiducial plug in its lid. The aperture assembly team replaced the plug with a flight blocking filter after the dewar was closed. The flex cables extending in the two-o'clock and eight-o'clock directions are the thermal straps and transition cables carrying signals from the first stage JFET amplifiers. At the end of transition cables are transition boards at the inner vapor cooled shield interface.
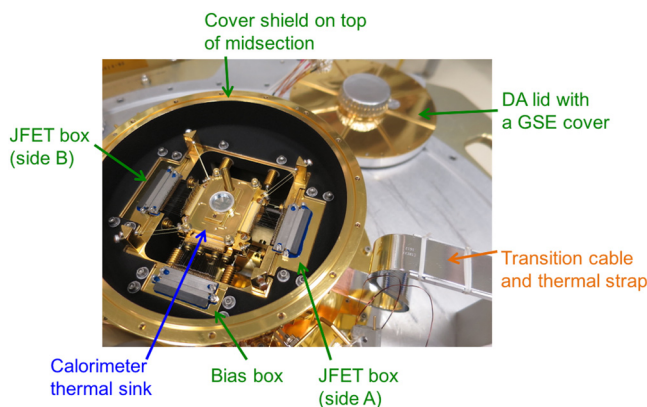
Fig. 2 The DA without the DA lid reveals the Kevlar® suspension and tensioned wiring in the midsection. The transition boards are not shown in this figure. Color of annotation text indicates the subassembly's operating temperature: blue for 50 mK, green for nominal 1.3 K, and orange for nominal 26 K.

performance will be discussed in detail elsewhere in this proceeding.[1,8,9,10,14]

For risk reduction, the PSP and the XBOX can control the calorimeter array as four quadrants of nine channels sharing one bias voltage each. The PSP and the XBOX also process the calorimeter signals in two halves, with dedicated electronics for each half (i.e., side A and side B). The anticoincidence detector has two redundant readouts, one with each half of the calorimeter readouts, and an actual bias as the sum of two independently controlled bias voltages. The XBOX can control the power to the four JFET packages independently, but JFETs on the same side have one common drain voltage setting. We will highlight some improvements or changes in the DA based on Suzaku XRS lessons learned and our engineering build in the following sections. Following the block diagram in Fig. 3, we will start

from the CTS at 50 mK and move outward toward the warmer modules.

2 Calorimeter Thermal Sink (at 50 milliKelvin)

The calorimeter array is the eye of the x-ray calorimeter spectrometer (XCS), and the CTS provides a mechanical and thermal enclosure with shielded passageways for electrical power and signals. It is thermally isolated from the 1.3 K midsection using 195 denier DuPont Kevlar® aramid fibers (from the same lot used for Suzaku) and contains three Kyocera ceramic electrical feedthroughs, a thermometer housing, and a BeCu flexure for the detector fan-out boards as shown in Figs. 5(a)–5(c). The CTS lid as shown in Fig. 5(d) provides a radiation enclosure cover together with the CTS lid blocking filter and a mechanical mount for the calibration source. The BeCu flexure was installed but not used for the detector fan-out boards due to insufficient time for proper design qualification. A single 2-56 screw with a nominal 6 in-oz torque proved adequate force in Suzaku XRS to hold the detector fan-out boards securely as shown in Fig. 5(c). On the ends of the CTS are thermal straps to the first stage ADR. The basic design remains the same as in Suzaku XRS with some simple mechanical updates such as a slight increase in overall dimensions, an increased aperture diameter in the CTS lid for a larger field of view, the position and angle of the calibration source in the CTS lid for alignment to the calibration pixel, the tongue-and-groove features on the CTS and the CTS lid, a slight adjustment in the locations of the suspension pulleys and pistons for better alignment, and laser-engraved alignment marks for clarity. Several lessons learned from Suzaku and the Astro-H engineering model, which helped improve the flight DA while keeping some heritage design factors are discussed in more detail below.

2.1 Planar Calorimeter Thermal Sink Wiring

Suzaku XRS had a complicated two-layer electrical wiring at the CTS feedthroughs to accommodate the large footprint for 32 channels of load resistors at 90 MΩ (three 30 MΩ chips in series). When 100 MΩ wire-bondable Sichrome chip resistors in a relatively compact footprint of 0.040 in. × 0.040 in. × 0.010 in. (1 mm × 1 mm × 0.25 mm) became available at Mini Systems Inc. (MSI) during the DA engineering model development, we designed a more compact load resistor package to house 19 load resistors (half of the calorimeter array plus 1 anticoincidence readout) to simplify the integration and wiring process and to improve reliability. A thermal cycle was added to the MSI screening process to address resistor failure from epoxy cure at 100°C in the chip mounting process. To complete an integral design to achieve a single-layer planar layout for the CTS wiring of 36 calorimeter readouts plus 2 anticoincidence detector readouts as shown in Fig. 6(a), we also needed to modify the anticoincidence fan-out board, the calorimeter detector fan-out board, and the power–zero-reference-potential (power/ZRP) feedthrough.

Incidentally, Fig. 6(a) also shows one of the few rare moments when the calorimeter array was exposed in the CTS. The calorimeter array was covered almost all the time during the flight integration. Figure 6(b) is a close-up view to show the traces on the anticoincidence fan-out connecting the bias circuit from the power/ZRP feedthrough package to the load resistor feedthrough package using wirebonds. Also, visible in Fig. 6(b) are some alignment notches (of the same width as the wirebond pads) we added in the flight CTS to facilitate a more consistent
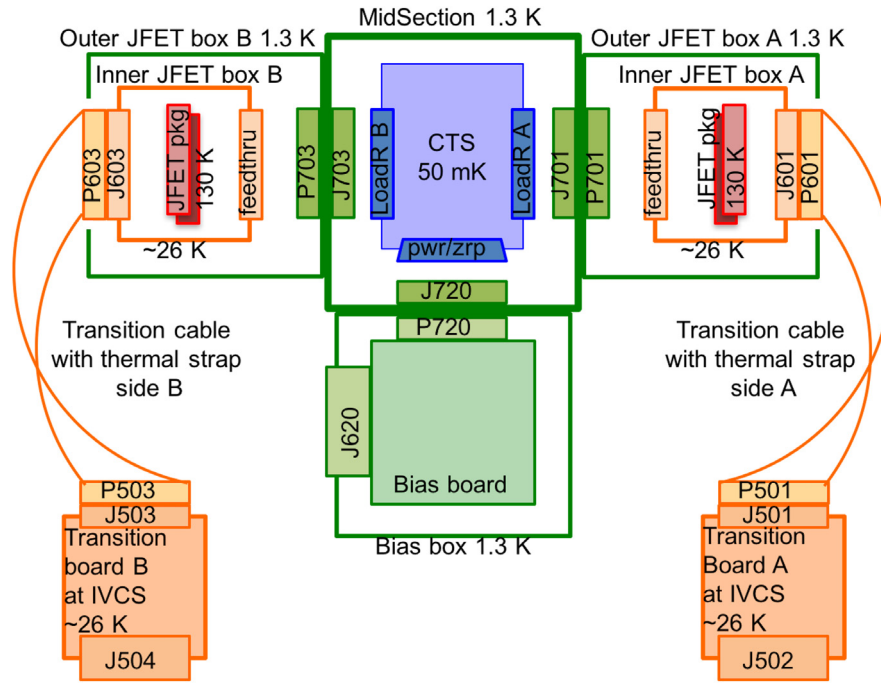
Fig. 3 A simplified DA block diagram shows modular interfaces and mating connectors in four temperature regions (by colors): 50 mK (blue), 1.3 K (green), 26 K (orange), and 130 K (red). Thermal isolation between the CTS and the midsection, between the inner JFET box and the outer JFET box, and between the JFET package and the inner JFET box are represented by gaps.
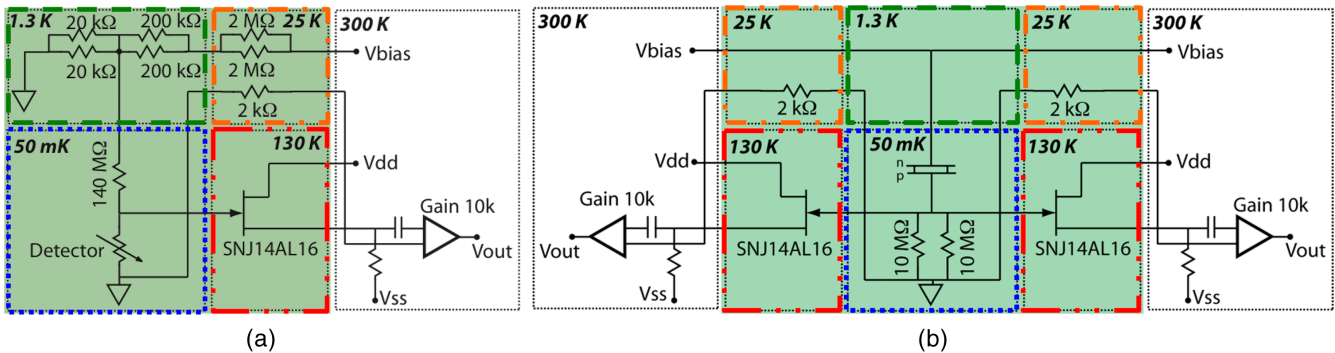
Fig. 4 Simplified readout circuit schematics for (a) the microcalorimeter and (b) the anticoincidence detector. The shaded regions indicate the part of analog read-out circuits in the DS. Different color boundaries are used for easier identification of temperature regions, 50 mK (blue), 1.3 K (green), 26 K (orange), and 130 (red).

assembly of the three feedthroughs and two detector fan-out boards.

The power/ZRP feedthrough passes the bias voltages for the calorimeter and anticoincidence detectors as well as the zero reference potential, which is also connected to the feedthrough's internal ground plane and exterior metallization and then to the CTS housing by silver epoxy and wirebonds. The power/ZRP feedthrough also provides the soldering pads for the CTS thermometer wires on its bottom side as shown in Fig. 7. Its trapezoid shape is a compromise between the available CTS space and fabrication limitations. An internal ground plane separates the thermometry signals from the bias voltage inside the power/ZRP feedthrough. Figure 8(a) shows a fully populated and wirebonded load resistor package. Provided the wirebonds are lower than the package depth at room temperature, the detector signals will not be shorted by the gold-plated Kovar lid at 50 mK

because alumina contracts less than gold. To maintain the overall suspension design in the DA midsection, the same as in Suzaku XRS, the overall load resistor package dimensions are constrained by key mechanical features in the CTS. The load resistor for the anticoincidence detector is placed at the center of the package to provide mirror symmetry in the package layout such that it can be used on both sides of the CTS. This is different from Suzaku XRS in which the load resistor of the anticoincidence detector was positioned at the end of the feedthrough.

IV curve measurements (using known 30 MΩ Nichrome thin film resistors in place of the calorimeter detectors) were collected during the DA functional test after the DA workmanship vibrational test to verify the load resistor values on 21 of 36 readout channels at 50 mK. The results shown in Fig. 9 indicate 134 $\pm$ 2 MΩ at 50 mK (versus Suzaku XRS Nichrome load resistors of three 30 MΩ in series or 90 MΩ at 60 mK). Within
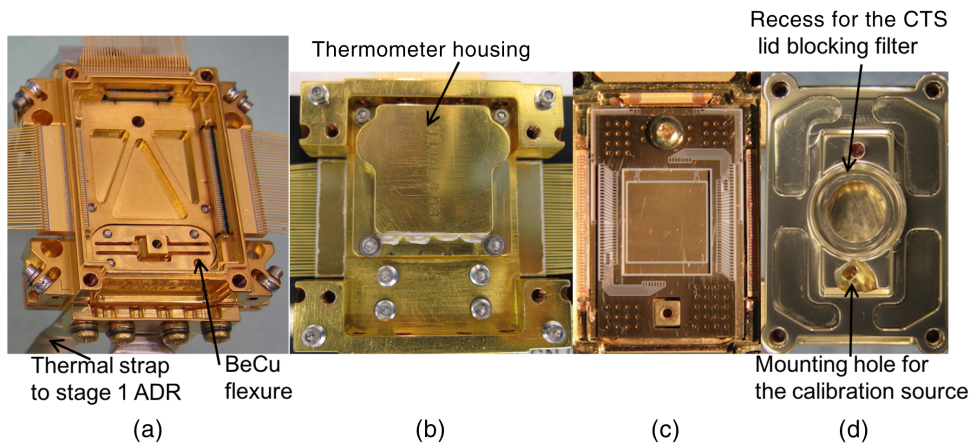
Fig. 5 (a) Top view of the CTS, (b) bottom view of the CTS, (c) zoomed view of the CTS cavity with unpopulated fan-out boards, and (d) the CTS lid without a radiation-blocking filter or the calibration source.
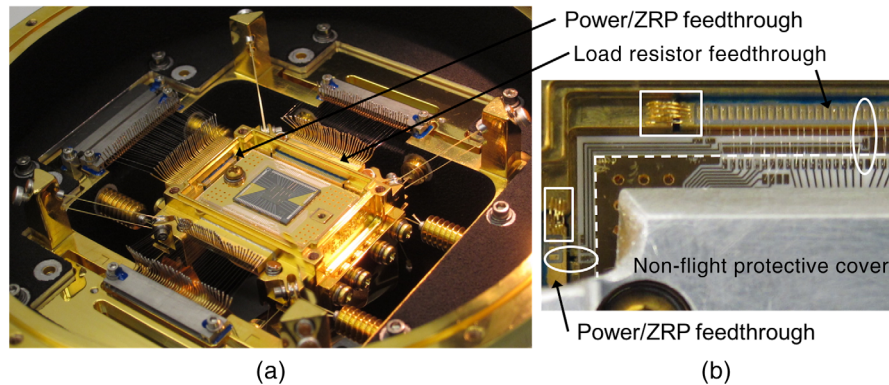
Fig. 6 (a) CTS with detectors at the 50 mK stage suspended and wired in the midsection. (b) A zoomed-in view to show how the traces on the anticoincidence fan-out board complete the bias circuits between the power/ZRP feedthrough and the load resistor feedthrough. The anticoincidence fanout board is bigger and visible outside the white dash line boundary. The calorimeter fanout board is smaller and visible inside the white dash line boundary. The alignment notches to facilitate integration are shown in the middle of white ovals, and the ribbon bonds for heatsink in white rectangles.
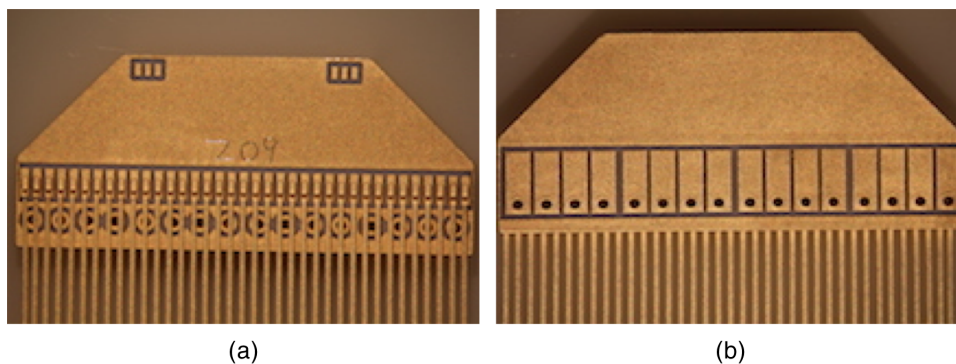
Fig. 7 The power/ZRP feedthrough package, (a) the top side showing the bias pads and the plated through-hole vias from the solder pads underneath and below the package leads and (b) the bottom side showing the thermometer wire soldering pads.

the CTS temperature control requirement of 2.5 μK RMS, the variation in the load resistance is only 50 to 150 Ω, or nominally 1 ppm, and not expected to introduce any significant bias voltage noise. However, the actual temperature sensitivity, dR/dT, may be slightly greater because the load resistors may be self-heated below 100 mK at the bias currents used in our measurements. Because the load resistors are now closer to the calorimeter array, to minimize thermal radiative impact from the midsection, gold ribbon bonds as shown in Fig. 6(b) are added to all three feedthroughs. Similarly, gold wirebonds

(a)   (b)
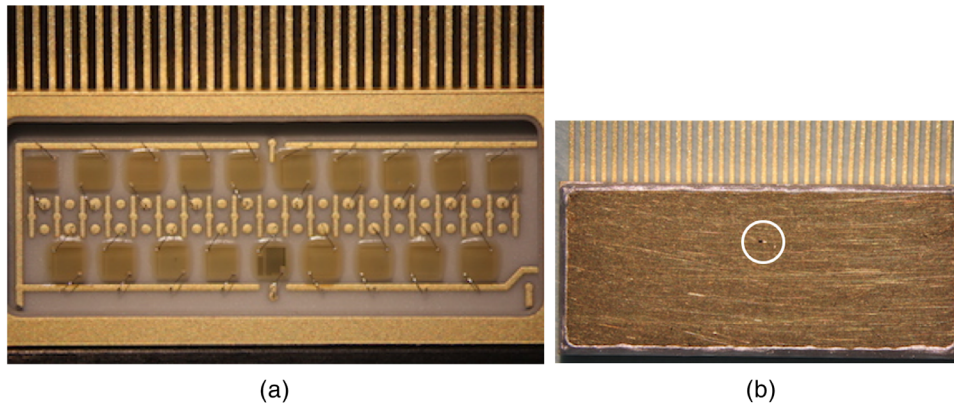
Fig. 8 (a) A fully populated and wire-bonded load resistor package. The bigger round pads are connected to the gate leads of the JFETs, and the horizontal bus lines provide the bias voltages. The smaller dots and vertical traces with tiny dots are connected to the ground plane (located between bus voltage and gate signals), the return lines, and the package's exterior metallization. The darker and slightly smaller chip resistor in the middle is the 5 MΩ Nichrome load resistor for the anticoincidence detector, and the other 18 chip resistors are Sichrome 100 MΩ load resistors for the calorimeter detectors. (b) The load resistor package is covered by a gold plated Kovar lid with a tiny vent hole (at the center of the white circle).

(a)   (b)
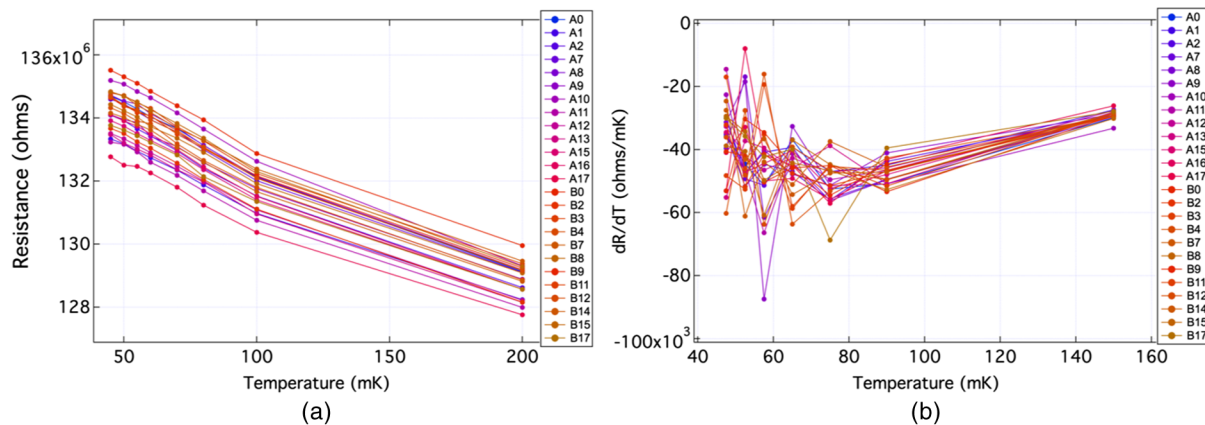
Fig. 9 (a) Resistor resistance versus temperature and (b) dR/dT versus temperature for the SXS Sichrome load resistors.

are added on the detector fan-out boards to CTS to provide heatsink to the CTS. Using the detector heat-sink measurements from Suzaku as a basis, we estimate the thermal conductance of the gold ribbon bonds to be 40 μW/K for each load resistor feedthrough package, and 20 μW/K for each power/ZRP feedthrough package.

2.2 Detector Heat Sink

Cosmic rays on the silicon calorimeter array frame introduce thermal perturbations to the calorimeters, and those perturbations were found to degrade the calorimeter performance in Suzaku XRS. Therefore, an efficient thermal path from the silicon detector chip to the CTS housing was included in the design for the detector fan-out boards. On the calorimeter fanout board, a continuous gold-plated heat-sink region was achieved using plated through-hole vias between the top and bottom gold-plated regions on the board. Because the calorimeter fan-out and anti-coincidence fan-out are stacked, there are two unplated, keep-out stripes at the bottom surface of the calorimeter fan-out to prevent shorting to ground. The

anti-coincidence fan-out has gold plating primarily on the top surface, but also has a small section of gold plating on the bottom surface by the 2-56 screw clearance hole for direct contact to the CTS housing. The gold-plated regions on the two surfaces of the anticoincidence detector fan-out board are also connected by plated through-hole vias. Figure 10 shows the top and bottom surfaces (bottom surfaces shown in mirror reflections) of the calorimeter array, and the anticoincidence detector fan-outs during inspection just before integration. The improved calorimeter performance is discussed by Kilbourne et al.[1]

2.3 Calorimeter Thermal Sink Thermometry

Inconsistencies in the CTS control thermometer readouts in Suzaku XRS were attributed to environmental radiative loading on the epoxy encapsulation. Therefore, the SXS CTS thermometers use a package with the sensor completely enclosed in the thermometer housing. The sensor wires are heatsunk to the thermometer housing before the thermometers are mounted at the bottom of the CTS. Instead of the ruthenium oxide temperature sensors used in Suzaku, neutron transmutation doped
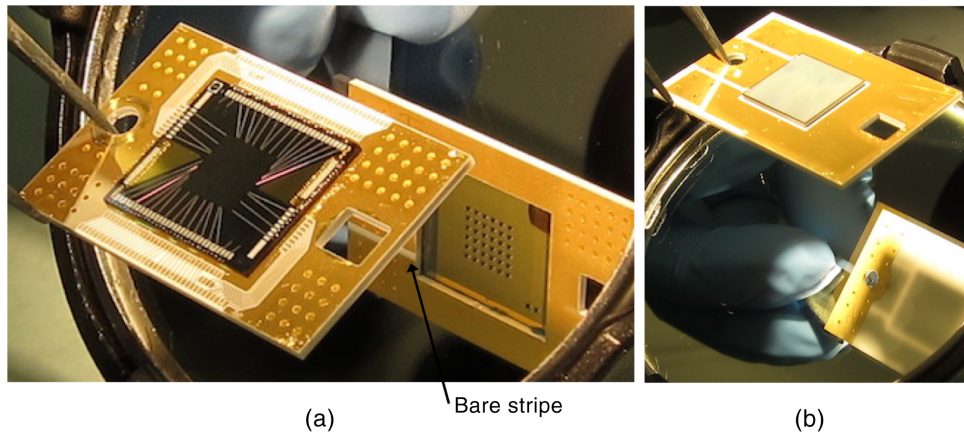
Fig. 10 Heat-sink gold plating on the detector fanouts. (a) The calorimeter array. A small unplated stripe is visible in the lower left portion of the mirror image. (b) The anticoincidence detector.
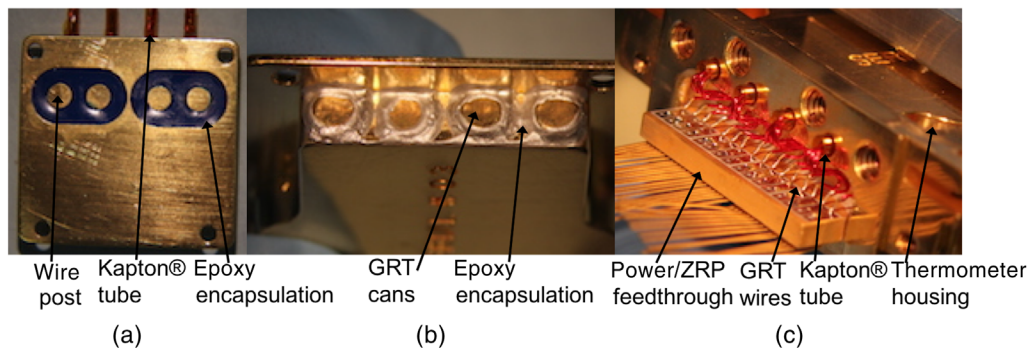
Fig. 11 Integration of CTS thermometers. (a) Bottom view of the thermometer housing shows the Stycast® 2850 encapsulation, (b) end view of the thermometer housing shows the H20E silver epoxy enclosure around the GRT canisters, and (c) end view of the CTS at the power/ZRP feedthrough package shows the GRT wiring.

germanium resistance thermometers (procured from Lake Shore Cryotronics) are used for their reliability and better sensitivity at 50 mK. Each set of four sensor wires are twisted together and wrapped around the heatsink post before being encapsulated with Emerson and Cuming Stycast® 2850 epoxy. Epoxy Technology Epo-tek® H20E silver epoxy is applied at the end openings as shown in Fig. 11. The wire pass-through holes and the heat-sink posts are lined with 0.001 in. thick Kapton® film to prevent chafing of the wire insulator sheaths. Because of the power/ZRP package design and assembly process, the thermometer sensor wires (with strain relief service loops) are soldered on a ceramic substrate at a confined location. For quality assurance to minimize risk of electrical short, caution was taken to keep solder clear of the plated through-hole vias because the package leads are only 0.010 in. above the package surface. It is also important to check the thermometer readout at every step of the installation for electrical shorts because the insulator sheath can chip or break during assembly. The flight thermometer resistance values range from 50 to 80 kΩ at 50 mK with a sensitivity ranging from −4.4 to −7.2 kΩ/mK. Based on housekeeping trending data in Fig. 12 from the Suzaku commissioning phase in-orbit, the CTS monitor thermometer readings showed a strong correlation to the helium tank temperature but only weak correlation to the inner vapor cooled shield (IVCS) temperature, whereas the control thermometer was held steady at 50 mK during ADR control. We postulate that despite the

improvement to heatsink 2.5 to 3 in. of the thermometer wires, the thermometers still experienced a differential conductive loading.

2.4 Minimizing Radiation Field Within the Calorimeter Thermal Sink Cavity

Differential gain was observed in the Suzaku XRS calorimeter array, suggesting differential radiative loading inside the CTS cavity from higher temperature stages, most likely the midsection.[19] As mentioned in our 2010 paper,[18] an absorbing layer for microwave frequency radiation was added inside the CTS lid as shown in Fig. 13. It is an epoxy layer nominally 1-mm thick of Stycast® 2850 loaded with lampblack carbon powder 8% by mass. This mix ratio is the maximum fraction of carbon powder we could incorporate evenly into the Stycast® 2850 epoxy while keeping the mixture workable. It is important to make sure the grooves in the lid and the keyway for the calibration source holder are completely clean to preserve the intended calibration source spot location on the calorimeter array. Despite this change, differential gain was still observed on the calorimeter array from data both on the ground and in orbit during initial cool down as described by Leutenegger et al.[9] and Porter et al.[14] in this proceeding. The CTS lid filter (procured from Luxel) was mounted at GSFC using Luxel's recipe after the lampblack/Stycast® layer was complete.
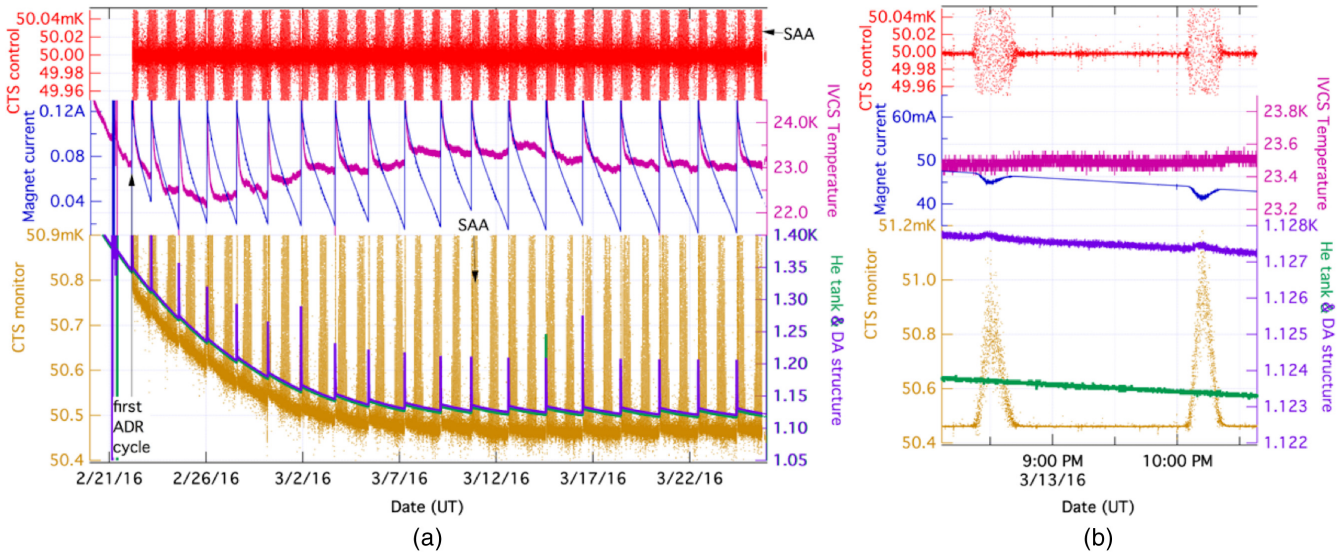
Fig. 12 (a) Housekeeping trending data from in-orbit operation day 5 ($Y + 5$) through day 37 ($Y + 37$). The top trace represents the CTS control thermometer. The middle two traces represent the stage 1 ADR control current and the IVCS temperature. The bottom three traces represent the monitor thermometers for the CTS, helium tank, and DA structure. The helium (He) tank and the DA structure are very close in temperature, and not easily distinguishable in this scale. (b) Zoomed-in view during two representative passes through the south Atlantic anomaly.

Fig. 13 The inside surface of a CTS lid with a 1-mm-thick layer of Stycast® 2850 loaded with lampblack carbon powder.

Fig. 14 Thermal conductance versus temperature of the DA CTS-to-ADR thermal straps.

2.5 Calorimeter Thermal Sink Thermal Strap

A thermal conductance requirement of 0.1 mW/K at 50 mK is imposed on the CTS thermal strap to optimize the duty cycle of the two-stage ADR operation at 50 mK. We used the same gold foil (4N Sigmund-Cohen 0.003 in. thick) as in Suzaku XRS, and measured 0.064 mW/K at 50 mK (versus Suzaku XRS 0.14 mW/K at 60 mK), which failed the thermal conductance requirement. We verified the residual resistance ratio (RRR) of the gold foil as-spooled to be 22.3, and 28 after 2 h of annealing at 700°C in vacuum, much lower than expected for high purity gold. For the flight DA, the CTS thermal straps were made of gold-plated copper foil because the as-spooled samples of the ESPI 4N copper foil 0.005 in. thick used for other ADR thermal straps gave an RRR value of 240 from the first batch and 155 from a second batch. The resulting thermal conductivity was better than 0.5 mW/K at 50 mK as shown in the thermal

conductance plot in Fig. 14. This, however, was not sufficient to mitigate the noise problem at frequency lower than 15 Hz due to microvibrational heating of the CTS as discovered in the engineering model.

2.6 Calibration Source

The University of Wisconsin provided a 55Fe source for internal use to the CTS cavity, which was tested for flight acceptance at Goddard Space Flight Center (GSFC), same as for Suzaku XRS. A minute amount of 55Fe radiative material at the end of a nickel wire is encapsulated in two pieces of 304 stainless steel, thin-walled tubing, each with a separate beryllium window. The source illuminates the calibration pixel for continuous gain tracking throughout the mission lifetime, which is nominally 6 μCi and 5 to 6 counts per second on the calibration

CTS lid blocking filter   Calibration source capture nut

(a)   (b)   (c)   (d)
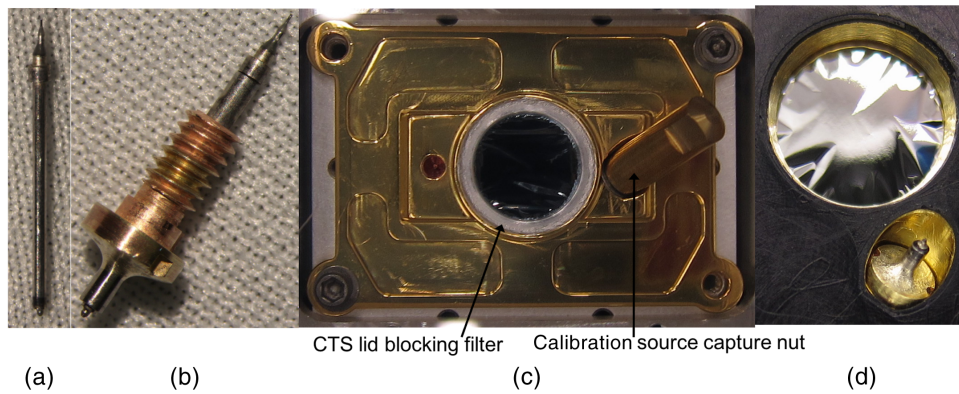
Fig. 15 (a) The calibration source before installation, (b) the calibration source mounted in its holder, (c) a top view of the CTS lid integrated with a calibration source and a CTS lid filter, and (d) an zoomed inside view of the CTS lid shows the calibration source below the CTS lid filter.

pixel at the time of launch. Figure 15 shows the calibration source and the source holder at different stages of integration and the final source position installed in the CTS lid after the CTS lid filter is mounted.

3 Midsection (at 1.3 Kelvin)

The midsection is basically a modular box frame for the mechanical and electrical interface at 1.3 K and is, for the most part, the same as for Suzaku XRS. There are some minor adjustments in the locations of the suspension features for better alignment. Figure 16(a) shows a bare cover shield seated on a bare midsection for reference. The midsection together with the bias box and JFET boxes form a light tight enclosure with the cover shield via a tongue-and-groove design. The groove feature is shown in Fig. 16(b). A layer of LORD Corporation Aeroglaze® Z306 paint with microglass spheres is applied to the interior surfaces of the midsection to reduce microwave frequency radiation in the cavity. This coating is also applied to the interior surfaces of the cover shield and the DA lid. A bake out at 100°C for more than 24 h is performed for molecular contamination control before suspending the CTS in the midsection module. The midsection door has a nominally

2-mm-thick layer of lampblack/Stycast® to further reduce the radiation field in the cavity.

A wiring diagram for the midsection, including reference to the detector pixel numbers, is shown in Fig. 17. To minimize thermal conduction, 0.0008 in. diameter CuNi-clad/NbTi-core wires with measured break strength of 28 gram force are used to complete electrical wiring because NbTi is superconducting at 50 mK. The NbTi core is 0.00074 in. in diameter and has a density of 6.55 g/cc. The CuNi cladding has an annular thickness of ~0.00003 and a density of 8.95 g/cc. Witness samples were made for quality assurance and evaluation of variations. The thermal conduction load from the midsection to the CTS through 20 Kevlar® threads and 111 NbTi flying leads is estimated as 0.25 μW. Wiring witness samples were made using an Astro-E2 spare midsection (the connector and feedthrough leads remain the same in Astro-H) before and after each soldering session for tension measurements. Wire lengths can vary depending on the position. Table 1 shows tension measurements and resulting first resonance frequency for the NbTi flying leads, which are all higher than 5 kHz, well beyond the first mechanical resonance of the CTS (333 Hz by model, and indirectly measured to be about 320 Hz during on-ground microvibration noise measurements[15]).

Midsection Cover shield Light seal   Light seal   Suspension Suspension
                          groove   groove   piston   screw
              (a)   (b)
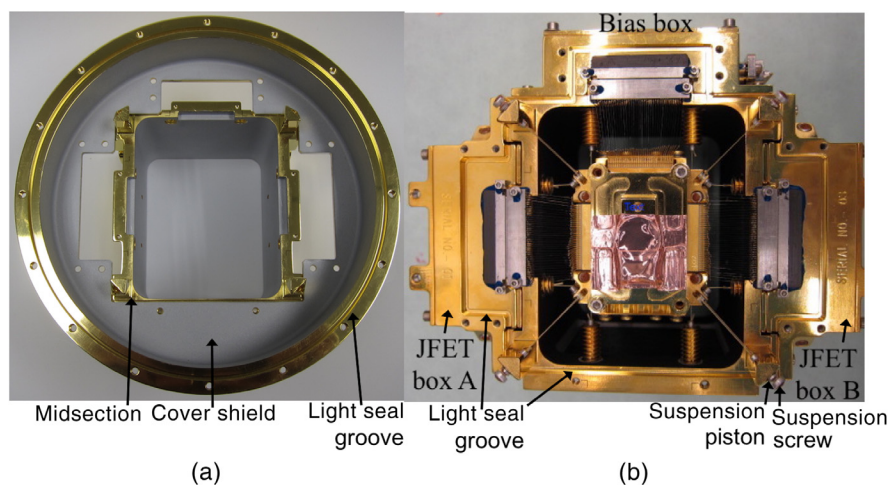
Fig. 16 (a) Top view of a bare cover shield seated on a bare midsection and (b) top view of the midsection integrated with the bias box and JFET boxes. The black interior surface in the midsection is the Z306/microsphere coating.
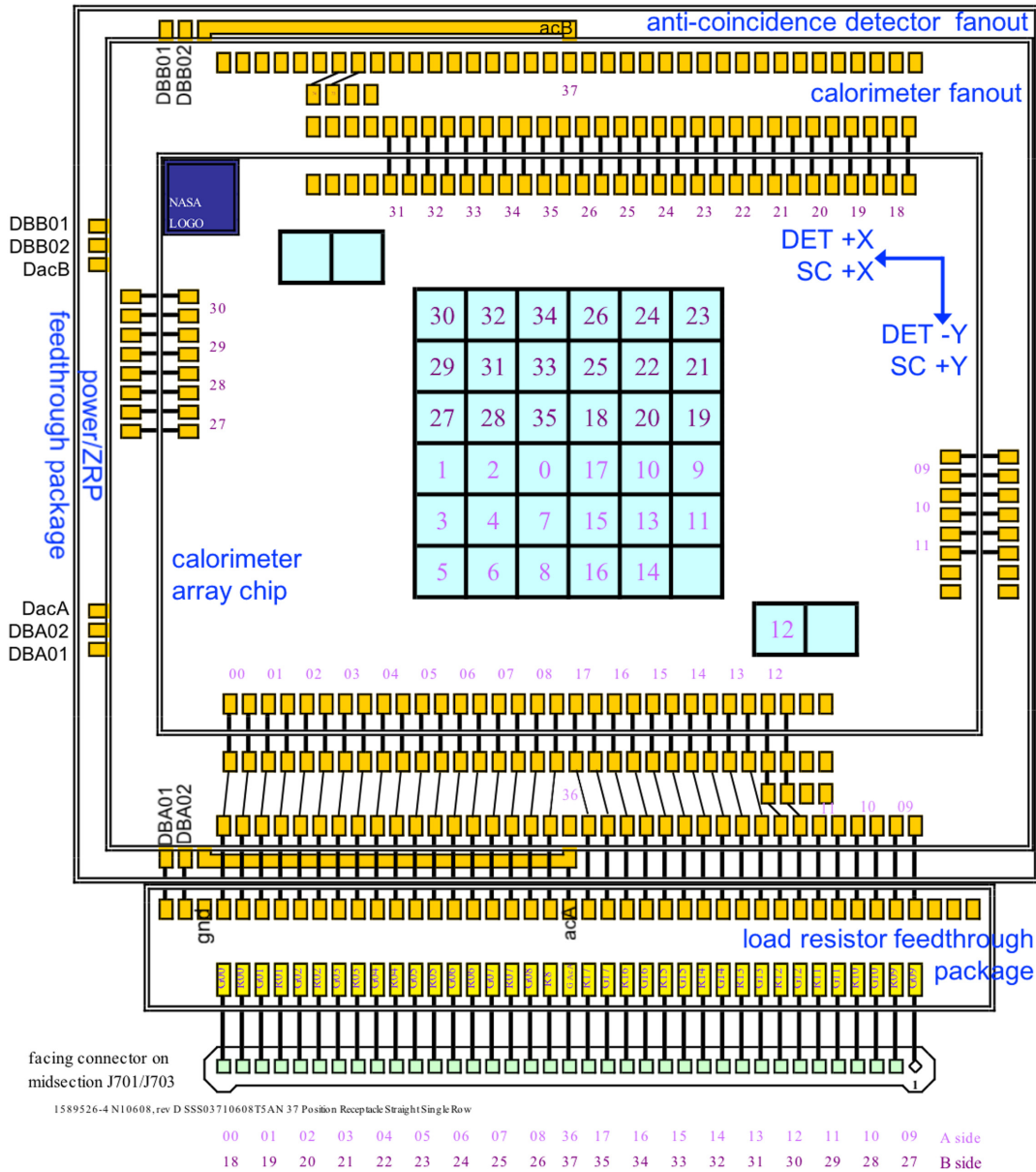
Fig. 17 Wiring diagram from the CTS to the midsection, and the pixel map corresponding to the nadir view of the calorimeter array. The anticoincidence detector signal on A side is channel 36, and on B side channel 37.

Table 1 Tension measurements and fundamental resonance frequency of flying leads in the CTS.

CTS	Average length L (mm)	ΔL (mm)			Average tension force F (grams force)	ΔF (grams force)	Fundamental frequency f (Hz)	$\Delta f/f$ (%)
Side A	13.1	0.34	FM	Side A	6.1	1.1	6321	12
Side B	13.1	0.51		Side B	4.3	0.80	5268	13
Power/ZRP	9.9	0.79		Power/ZRP	6.3	0.56	8485	12
			FM spare	Side A	6.4	0.85	6445	9
				Side B	7.8	0.91	7109	10
				Power/ZRP	7.9	1.3	9451	16
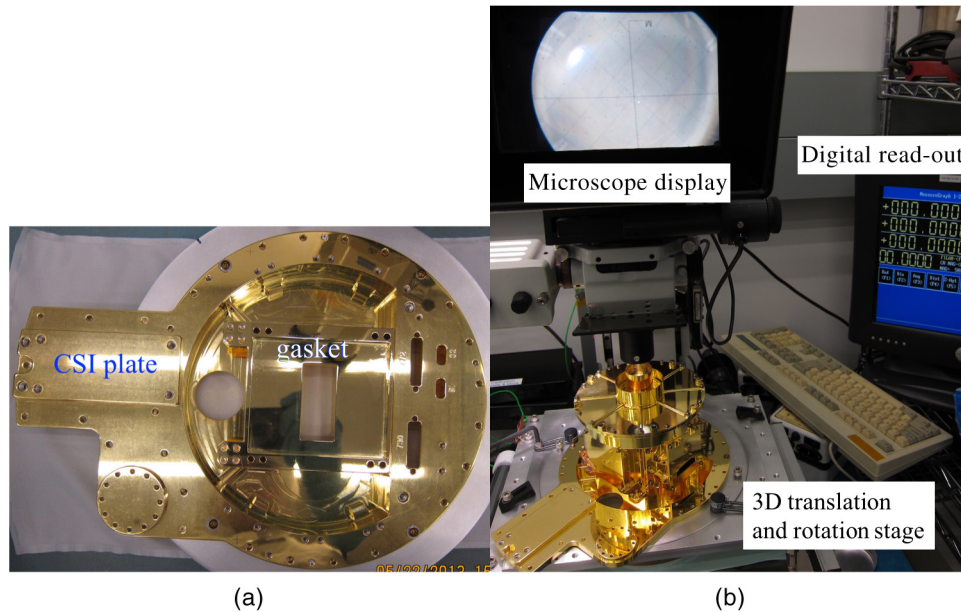
Fig. 18 (a) The CSI plate with the copper gasket on top. (b) The same Dynascope setup for the DA lid alignment and verification measurements. The center of the microcalorimeter array as the reference zero position is shown in the display monitor.

3.1 Bias Box

The bias voltage divider resistors inside the bias box are MSI Nichrome thin-film surface-mount resistors instead of the wire bondable chip resistors in Suzaku XRS. The voltage divider is made with two parallel 200 kΩ resistors and two parallel 20 kΩ resistors connected in series. The bias divider also includes two parallel 2.2 MΩ resistors in the detector bias supply harness at the IVCS interface. The divider ratio of the bias voltage setting to the bias voltage at the calorimeter detector is 121. The thermometry, bias, and zero reference potential are all now in one MDM69 connector due to limitation in accessibility, rather than two HD44 connectors as in Suzaku XRS. A Lake Shore Cernox temperature sensor is mounted in the bias box to monitor the DA temperature.

3.2 Cover Shield

The cover shield is unchanged from Suzaku XRS and interfaces with the DA lid to form a light tight enclosure. The mounting hole pattern is updated to match the slight changes in the midsection, the bias box, and the JFET boxes. As shown in Fig. 16(b), the suspension screw heads on the midsection posts are beyond the groove footprint. Consequently, the cover shield must be rocked in and out of position carefully to clear the suspension screw heads.

3.3 Calorimeter Spectrometer Insert Plate Interface

In contrast to a small aluminum interface plate to the helium tank in Suzaku XRS, the midsection is mounted on the CSI plate with a copper gasket in between for an isothermal joint. Figure 18(a) shows the gasket on top of the CSI plate. The CSI plate also serves as a heatsink to the stage 3 ADR. The CSI plate, made of aluminum, was designed by GSFC, fabricated by SHI, and gold plated at GSFC. The gasket, made of copper, was designed and fabricated at GSFC. Copper tape was used to cover some loose gaps between the gasket and

midsection to minimize thermal radiation leakage. The gasket includes two mounting points for thermometers to monitor the thermal interface.

3.4 Detector Array and Detector Assembly Lid Alignment

The DA was mounted on the CSI plate once the DA subsystem performance tests and calibration were complete. A nonflight transparent fiducial plug was designed and used to facilitate aligning the DA lid to the center of the microcalorimeter array. Two other fiducial plugs were designed and made for a slip fit in the CSI plate alignment pin holes to determine the virtual center of the CSI plate, which is also at the center of the helium dewar. Figure 18(b) shows the optical inspection microscope, Dynascope model-5D, with four degrees of freedom for the optical alignment process and verification measurements. The detector array was transferred to an intermediate fiducial plate on the cover shield and then aligned to the DA lid. The DA lid and the cover shield were match drilled, and their alignment was verified by measurements. The final alignment measurements showed the center of the detector array at $(-0.04, 0.01) \pm (0.03, 0.03)$ mm with respect to the CSI plate virtual center in the dewar XY coordinate system (the same as the spacecraft XY).

4 JFET Amplifiers (at 130 K), JFET Boxes, Transition Cables

The first stage JFET amplifiers operate at 130 K for minimal noise. An estimated 2 eV full width half max was allocated to the JFET noise in the calorimeter detector noise budget, and that amounts to 9 nV/$\sqrt{\text{Hz}}$ white noise and $1/f$ noise of 16 nV/$\sqrt{\text{Hz}}$ at 10 Hz. Same as in Suzaku XRS, two JFET packages are attached to a carrier tray which is doubly suspended as shown in Fig. 19(a). The carrier tray is suspended first using 55 denier Kevlar® fibers from the inner JFET box, which is heatsunk via the transition cable thermal strap to the
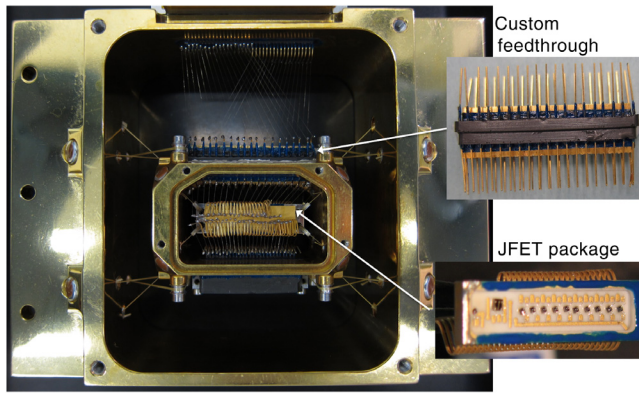
Fig. 19 Double suspension and wiring of the JFET amplifiers in nested outer and inner JFET boxes. A JFET package is attached to the suspended carrier tray with Stycast® 2850 and silver epoxy H20E on the interface for grounding. The inner JFET box has a custom feedthrough with double ground planes in the middle.

IVCS at 26 to 28 K. The inner JFET box is suspended using 195 denier Kevlar® fibers from the outer JFET box, which is heat-sunk to the helium tank. Figure 20 shows the wiring diagram inside the outer JFET box, including the inner JFET box and the JFET packages. From the inner JFET box to the transition board, there is a one-to-one connection with a 2 kΩ resistor on each source return line. CuNi clad, SS316 core, 0.00068″ diameter wires with core density of 7.97 g/cc, clad density of 8.95 g/cc, and measured break strength of 43.4 gram force are used to minimize thermal conduction between the JFET package, the inner JFET box, and the outer JFET box. Wiring witness samples were made for quality assurance and evaluation of variations. A conductive load of 250 μW is estimated between the two JFET boxes and the helium tank through the 12 Kevlar® threads and 37 SS316 flying leads from each inner JFET box to its outer JFET box and thus the midsection. Total heat load on the IVCS from the inner JFET box is estimated to be 15 mW during normal operation.

4.1 JFETs and the JFET Package

Ten JFETs, one temperature sensing diode, and one resistive heater are mounted and screened in each JFET package. Two JFET packages are attached to the carrier tray, using Stycast® 2850 and silver epoxy H20E, as shown in Fig. 19(b) for a common electrical zero reference potential, after suspension in the inner JFET box is complete. The dimensions of the JFET package remained the same as Suzaku XRS while accommodating one more JFET with one additional pair of leads on each package. An exterior metallization connected to an electrical ground (here also the zero reference potential) was added to provide shielding. The JFETs were from the same lot of InterFET SNJ14AL16 for Suzaku XRS and were screened at room temperature for similar characteristics of interest, in this case the saturation current at zero gate-source voltage (Idss, or maximum current from drain to source) and the output impedance (Z). The selected JFETs were then mounted in the JFET package, screened for minimal noise at 130 K in the range from 10 to 100 Hz, and replaced as needed. Table 2 lists the characteristic parameters and noise performance of the JFETs for the flight DA. Data on representative JFET gain were also collected via IV curve measurements with open inputs instead of resistors during the DA functional test, showing an average gain of

0.992 ± 0.003. Figure 21 shows the power levels from the JFET packages at 130 K. The total power is <12 mW. Also, the JFET package heater power levels drop as the IVCS temperature increases during the ADR recycles. Noise spectra from the last cold aliveness test during cool down before launch were all nominal and better than requirements as shown in Fig. 22. In-orbit JFET noise trending data in Fig. 23 show an increase in low-frequency noise for JFET #35 on Y + 4 before the detectors reached 50 mK on Y + 5. As a result, calorimeter pixel 35 had worse resolution than others in the array. Unfortunately, we lack noise records on the third day of operations to identify a trigger or correlated event due to an operation planning error. More details on in-orbit SXS performance are discussed by Porter et al.[14]

4.2 Inner JFET Box

The 55 denier Kevlar fibers used to suspend the JFET packages inside the inner JFET box were from the same lot used for Suzaku XRS. Pull tests were repeated and indicated a break strength of 1.07 ± 0.05 kilogram force. There are several changes from Suzaku XRS. Built-in guide holes replaced guide corners attached at the two ends of Teflon® guide tubes. This leads to a change in the Kevlar fiber path in the outer JFET box. The feedthrough as shown in Fig. 19(c) has two ground planes in the middle instead of two rows of position matching pins. Although the ground planes should be connected to the Xbox zero reference potential, same as the JFET returns, due to a build error the ground planes are instead connected electrically to the IVCS through the inner JFET boxes and the transition thermal straps. Nevertheless, the IVCS is connected electrically to the dewar main shell by the internal helium plumbing, and so should have the same zero reference potential as the Xbox, albeit via a different path. We did not observe any clear evidence that this change introduced additional noise pickup. Since the Nanonics 55-pin connector was still used for the inner JFET box, an increase in the two channels on each side required removing redundancy on the JFET package thermal control. Finally, instead of thermal strap being permanently attached by silver epoxy H20E from the inner JFET box to the transition box, the thermal strap is now removable, making the handling of the JFET boxes easier. Table 3 shows our measurements and results of the fundamental resonance frequency for the SS316 tensioned leads in the inner JFET boxes, and they are all higher than 10 kHz.

4.3 Outer JFET Box

The outer JFET box changed little from Suzaku XRS. The 195 denier Kevlar® fibers were from the same lot used for Suzaku XRS. Pull tests were repeated and indicated the break strength to be 3.8 ± 0.2 kilogram force. As mentioned earlier, the routing of suspension yarns changed with the inner JFET box modification. Table 4 shows tension measurements and the resulting fundamental resonance frequency for the SS316 tensioned leads in the outer JFET boxes, which are all higher than 5 kHz.

4.4 Transition Board, Transition Cable, and Thermal Strap

A flex cable design is used for the transition cables, instead of the source-return twisted pairs in Suzaku XRS. Each transition board is mounted on a diving board bracket covered with
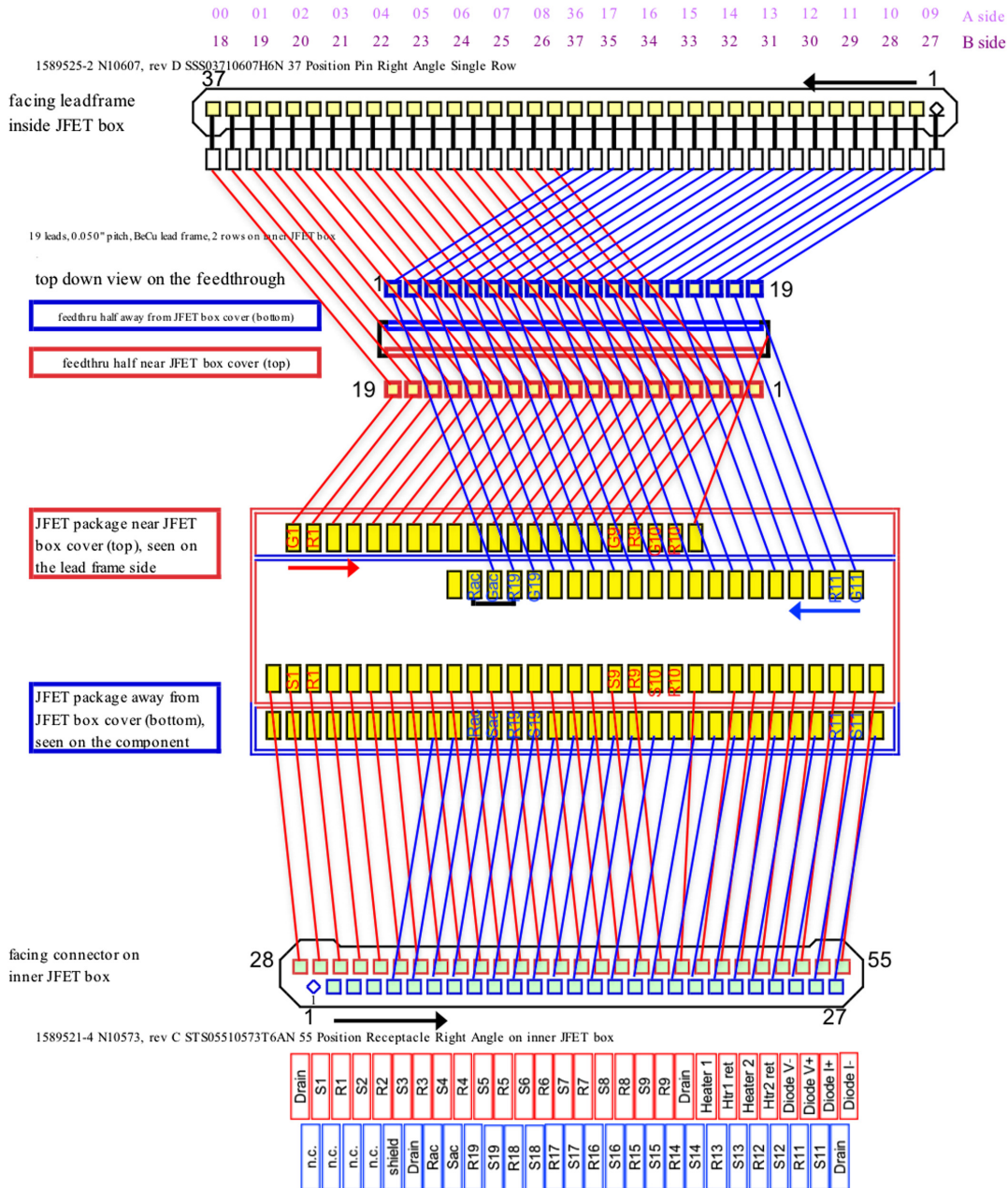
Fig. 20 Wiring diagram inside the JFET boxes.

Table 2 Characteristics measurements of JFETs selected for flight.

Astro-H	Saturation current at rmT	Output impedance at rmT	Noise 100 Hz at 130 K (nV/$\sqrt{\text{Hz}}$)		Noise at 10 Hz at 130 K (nV/$\sqrt{\text{Hz}}$)		DC source voltage at 2V bias at 130 K (V)	
Detector Pixel #	(mA)	(ohm)	Screen data	Final test data	Screen data	Final test data	Screening data	Final test data
0 to 8	1.677 ± 0.003	1680 ± 90	4.7 ± 0.3	5.5 ± 0.5	4.9 ± 0.5	5.5 ± 0.4	0.56 ± 0.01	0.56 ± 0.01
9 to 17, 36	1.694 ± 0.005	1730 ± 70	4.9 ± 0.4	5.6 ± 0.4	5.5 ± 0.4	5.7 ± 0.4	0.548 ± 0.006	0.545 ± 0.005
18 to 26	1.622 ± 0.001	1430 ± 40	4.7 ± 0.3	5.3 ± 0.2	5.0 ± 0.4	5.3 ± 0.2	0.528 ± 0.009	0.528 ± 0.007
27 to 35, 37	1.634 ± 0.003	1470 ± 20	4.9 ± 0.2	5.4 ± 0.3	5.3 ± 0.3	5.4 ± 0.3	0.527 ± 0.006	0.526 ± 0.006
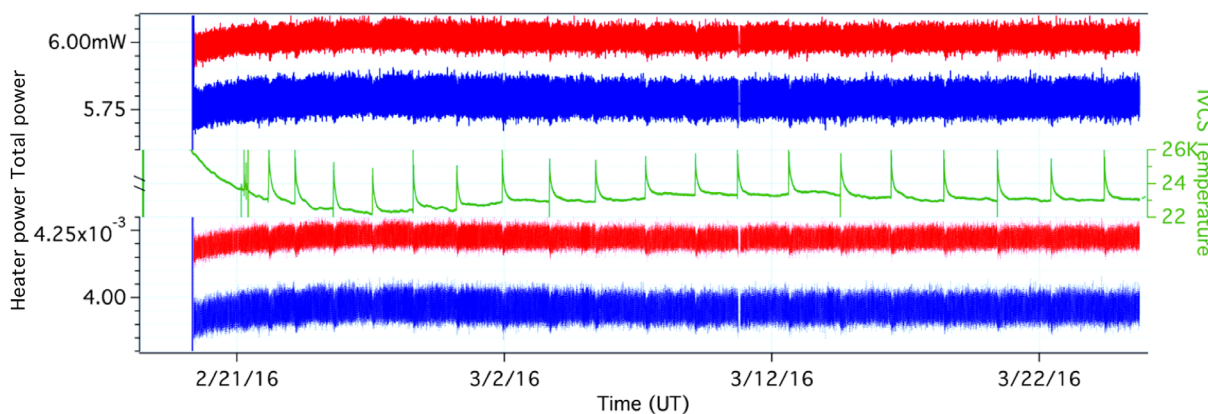
Fig. 21 Power levels from the JFET packages at 130 K, red for side A and blue for side B. The top set is total power, and the bottom set is the power from the JFET package heaters. The green trace is the IVCS temperature for reference. The drops in the power levels correspond to IVCS temperature increase during ADR recycles.
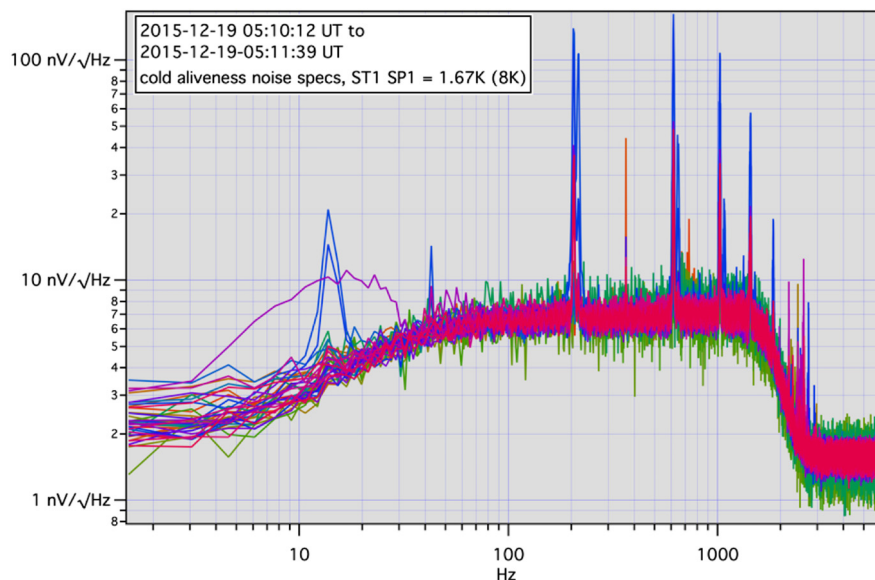
Fig. 22 JFET noise spectra from the cold aliveness test during the last cool down before launch, with the CTS at about 1.7 K and the He tank at about 1.5 K. Channel 28, shown in purple with a wide excursion from 3 to 30 Hz, suffered a glitch during this data run.

radiation shields for compactness. The transition board-bracket subassembly is anchored mechanically and thermally at the IVCS at the time of dewar integration. The transition cable and thermal strap are coated with vapor deposited aluminum (VDA) for lower emissivity. They are mated to the inner JFET box connector and the box cover, shaped for strain relief, mated to the transition board, and then secured on the diving board. Figure 24 shows a mock-up assembly of the transition cable and thermal strap assembly. The connector pins on the transition cables are exposed and are trimmed to specific length to prevent shorting with the transition board bracket. Also to prevent shorting with the transition board bracket, the part of the thermal strap next to the connector pins is not coated with VDA. A cutout in the outer JFET box cover was increased to clear the Nanonics connector and the thermal strap. The transition thermal strap is made of DuPont AP9222R. A pristine as-spooled sample has an RRR of 230, which is reduced to 190

after multiple severe manipulations, a reduction of ~20%. The thermal conductance is estimated to be 7 mW/K.

5 Susceptibilities and Lessons Learned

One major change from Suzaku to Astro-H was an increase in the number of pixels from 32 to 36. Some compromises were made due to limited available pins in the inner JFET box Nanonics 55-pin connector. Four channels (0, 9, 18, and 27) do not have ground pins on both sides, and therefore are more susceptible to noise pickup. Unfortunately, channel 0 and 18 are at the center of the calorimeter array. The anticoincidence readout channel was positioned in the middle of the load resistor feedthrough package because of dimensional limitations. As a result, the four nearest electrical neighbor channels (8, 17, 26, and 35) have cross talk pulses from the anti-coincidence detector. It was also necessary for the anticoincidence detector read-out to share a return with an adjacent calorimeter
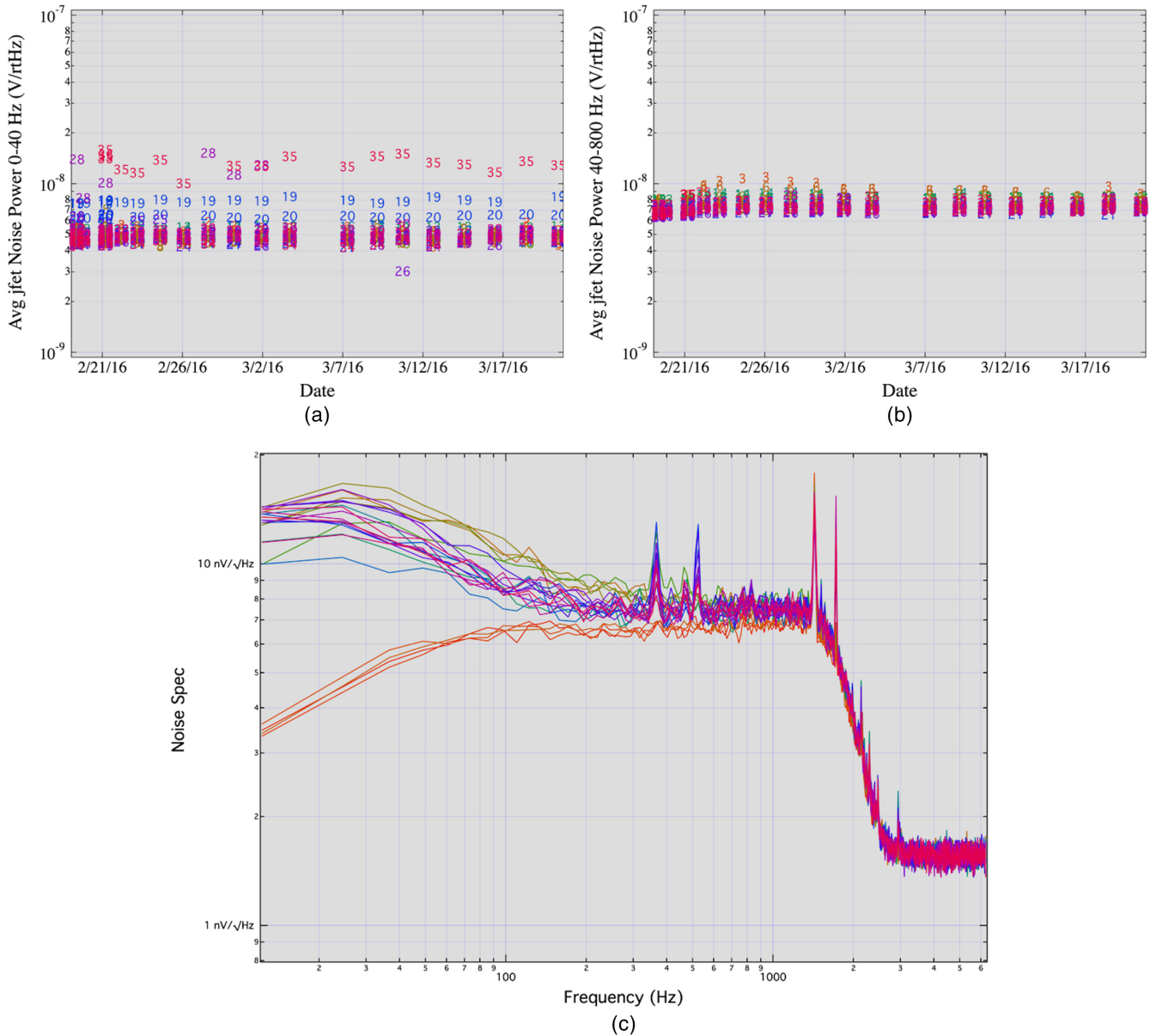
Fig. 23 In-orbit noise trend. The detector pixel or channel numbers are shown as markers. (a) JFET noise trend, power spectral density average in the range of 0 to 40 Hz. JFET #35 had higher noise than the group performance starting on February 21, 2016. (b) JFET noise trend, power spectral density average in the range of 40 to 800 Hz. (c) Representative in-orbit noise spectra on channel 35 at CTS temperature 1 to 1.5 K from $Y + 1$ to $Y + 36$. Noise increased significantly in the low frequency band starting on $Y + 4$.

Table 3 Tension measurements and fundamental resonance frequency of flying leads in the inner JFET boxes.

Average length L (mm)	ΔL (mm)			Average tension F (gram force)	ΔF (gram force)	Fundamental frequency f (Hz)	$\Delta f / f$ (%)
6.3	1.5	FM	SN01	3.6	1.1	11037	22
			SN03	3.6	1.3	11055	24
		FM spare	SN02	3.5	1.6	10798	30
			SN04	3.4	1.1	10694	17

Table 4 Tension measurements and fundamental resonance frequency of flying leads in the outer JFET boxes.

Average length L (mm)	ΔL (mm)			Average tension F (gram force)	ΔF (gram force)	Fundamental frequency f (Hz)	$\Delta f / f$ (%)
19.2	1.4	FM	SN01	9.6	2.8	5866	22
			SN03	8.2	2.0	5425	20
		FM spare	SN02	9.4	3.2	5809	24
			SN04	11.9	2.4	6513	17
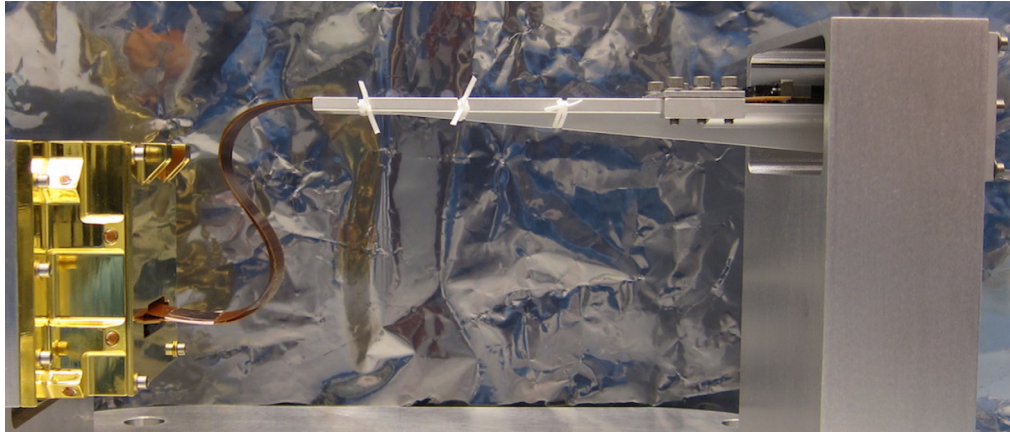
Fig. 24 A mock-up assembly of the transition cable, thermal strap, transition board to JFET boxes.

channel on the JFET package due to limited available pins in the outer JFET box Nanonics 37-pin connector. Two channels (17 and 35) seem to show more noise from the anticoincidence detector cross talk. Unfortunately, channels 17 and 35 are also at the center of the calorimeter array.

With the stage 3 ADR next to the DA, it was found necessary to limit the stage 3 ADR magnet current during the cryogen-free operation to not impact the calorimeter performance from suspected magnetic field leakage beyond the stage 3 ADR magnet shield. We have observed some other noise behaviors potentially related to the stage 3 ADR operation, but further investigation is needed to identify the actual cause.

A fit check of mechanical parts prior to installation proved useful. During testing of the engineering model, the calibration source in the CTS lid was discovered to be poorly aligned to the calibration pixel. A drawing review of the CTS lid and the calibration source holder revealed a mechanical interference between the key and keyway. We have also found it helpful to have witness samples before and after each tension wiring session in the JFET boxes and the midsection as additional practice and an assessment on the actual work.

6 Conclusion

We were able to incorporate many of the lessons learned from Suzaku XRS and our engineering build, and as a result, the flight build process was more streamlined with better reliability. Although there are some inevitable limitations, the overall performance exceeds expectations.

References

1. C. A. Kilbourne et al., "The design, implementation, and performance of the ASTRO-H SXS calorimeter array and anti-coincidence detector," *Proc. SPIE* **9905**, 99053L (2016).
2. G. A. Sneiderman et al., "Cryogen-free operation of the soft x-ray spectrometer instrument," *Proc. SPIE* **9905**, 99053N (2016).
3. P. J. Shirron et al., "Design and on-orbit operation of the adiabatic demagnetization refrigerator on the ASTRO-H soft x-ray spectrometer instrument," *Proc. SPIE* **9905**, 99053O (2016).
4. E. Yuichiro et al., "Porous plug phase separator and superfluid film flow suppression system for the soft x-ray spectrometer onboard ASTRO-H," *Proc. SPIE* **9905**, 99053P (2016).
5. C. A. Kilbourne et al., "The design, implementation, and performance of the Astro-H SXS aperture assembly and blocking filters," *Proc. SPIE* **9905**, 99053Q (2016).
6. H. Noda et al., "Thermal analyses for initial operations of the soft x-ray spectrometer (SXS) onboard ASTRO-H," *Proc. SPIE* **9905**, 99053R (2016).
7. R. Fujimoto et al., "Performance of the helium dewar and cryocoolers of ASTRO-H SXS," *Proc. SPIE* **9905**, 99053S (2016).
8. Y. Ishisaki et al., "In-flight performance of pulse processing system of the ASTRO-H soft x-ray spectrometer," *Proc. SPIE* **9905**, 99053T (2016).
9. M. A. Leutenegger et al., "In-fight verification of the calibration and performance of the ASTRO-H soft x-ray spectrometer," *Proc. SPIE* **9905**, 99053U (2016).

10. M. E. Eckart et al., "Ground calibration of the ASTRO-H soft x-ray spectrometer," *Proc. SPIE* **9905**, 99053W (2016).
11. T. Hayashi et al., "Point spread function of ASTRO-H soft x-ray telescope (SXT)," *Proc. SPIE* **9905**, 99055D (2016).
12. T. Takahashi et al., "The ASTRO-H x-ray astronomy satellite," *Proc. SPIE* **9905**, 99050U (2016).
13. R. L. Kelley et al., "The ASTRO-H high-resolution soft x-ray spectrometer," *Proc. SPIE* **9905**, 99050V (2016).
14. F. S. Porter et al., "In-flight performance of the soft x-ray spectrometer detector system on ASTRO-H," *Proc. SPIE* **9905**, 99050W (2016).
15. Y. Takei et al., "Vibration isolation system for cryocoolers of soft x-ray spectrometer onboard ASTRO-H," *Proc. SPIE* **9905**, 99050X (2016).
16. M. Tsujimoto et al., "In-orbit operation of the ASTRO-H SXS," *Proc. SPIE* **9905**, 99050Y (2016).
17. O. Takashi et al., "First peek of ASTRO-H soft x-ray telescope (SXT) in-orbit performance," *Proc. SPIE* **9905**, 99050Z (2016).
18. F. S. Porter et al., "The detector subsystem for the SXS instrument on the Astro-H observatory," *Proc. SPIE* **7732**, 77323J (2010).
19. R. L. Kelley et al., "The Suzaku high resolution x-ray spectrometer," *Publ. Astron. Soc. Jpn.* **59**(sp1), S77–S112 (2007).

Meng P. Chiao received her PhD in physics from the University of California, Los Angeles, in 1998. Currently, she is an instrument systems engineer at NASA Goddard Space Flight Center in the X-ray Astrophysics Recovery Mission (XARM) Resolve instrument, a science recovery mission for Astro-H (Hitomi).

Biographies for the other authors are not available.